

# Mechanically-Compliant Magnetoelectric Sutures for Wound Management

*Yi Yang, Ping Wen, Xingmei Chen, Yafei Wang, Shenglong Zhu, Zhipeng Ni, Lingfeng Yuan, Liangjie Shan, Pei Zhang, Pujing Shi, Boyuan Huang, Wenwen Liu, Yuewen Zhang, Ziyi Yu, and Ji Liu\**

**Sutures are the standard approach for wound closure and surgical incisions, but their clinical utility is constrained by inherent mechanical mismatch and the absence of multifunctional capabilities. While electrical stimulation has emerged as a promising nonpharmacological strategy for accelerated wound healing, achieving seamless integration of on-demand, untethered electrical stimulation with suture systems persists as a critical challenge. Here, a magnetoelectric suture is developed by incorporating core-shell magnetoelectric nanoparticles within a piezoelectric P(VDF-TrFE) matrix. Upon external magnetic field exposure, magneto-mechano-electric cascade synergistically generated a programmable electrical output, thereby enabling spatiotemporally controlled electrical stimulation at the wound site. The ME suture is engineered with a polyzwitterionic hydrogel skin, imparting them with improved mechanical compliance, biocompatibility, and reduced foreign body response, and enabling friction-minimized removal. In a rat incisional wound model, the ME suture with daily magnetic induction achieved significantly faster healing by reducing the recovery time from ten days to just five days. This work establishes a paradigm for intelligent suture systems, offering a theranostic platform that synergizes mechanoadaptive properties with electrically augmented tissue repair for next-generation wound management.**

## 1. Introduction

Medical sutures, the cornerstone of wound closure and surgical repair, serve to approximate tissues while minimizing infection and scarring through mechanical stabilization.<sup>[1,2]</sup> Despite the large global market (i.e., \$4.9 billion in 2023), traditional sutures, often made of plastic (i.e., poly(lactic-co-glycolic) (PLGA)

and nylon), proteins (i.e., collagen and silk) or metals (i.e., stainless steel wire), exhibit persistent limitations, including tissue trauma from piercing/removal, chronic inflammation, and scar formation due to stiffness mismatch,<sup>[1]</sup> and passive functionality in wound management.<sup>[3,4]</sup> Recent advancements in sutures have focused on embedding sutures with sensors for *in situ* monitoring the wound conditions, such as pH,<sup>[1]</sup> temperature,<sup>[2]</sup> and the wound integrity,<sup>[4]</sup> allowing for real-time feedback on infection risks and inflammation. Additionally, sutures formulated with drug-delivery systems have also been engineered to release therapeutics, such as antibiotics or growth factors, at the wound sites, thus promoting the wound healing and reducing the risk of infection.<sup>[5–8]</sup> However, these innovations remain constrained by their inability to actively modulate the wound microenvironment through programmable interventions.

Mostly recently, electrical stimulation (ES) has emerged as an effective nonpharmacological strategy for wound healing.<sup>[9,10]</sup> For example, external electrical field (i.e., 10–60 mV for the endogenous voltage) at the wound sites could effectively activate the migration of key cells, such as inflammatory cells, fibroblasts, and keratinocytes, thus improving the wound healing outcomes.<sup>[11,12]</sup> Sutures engineered with desirable electron conductivity have also shown great potential for transforming postoperative care and

Y. Yang, P. Wen, X. Chen, Y. Wang, Z. Ni, L. Yuan, L. Shan, P. Zhang, P. Shi, J. Liu

Department of Mechanical and Energy Engineering  
Southern University of Science and Technology  
Shenzhen 518055, P. R. China  
E-mail: [liuj9@sustech.edu.cn](mailto:liuj9@sustech.edu.cn)

P. Wen, Y. Zhang  
College of Chemistry and Chemical Engineering  
Lanzhou University  
Lanzhou, Gansu 730000, P. R. China

S. Zhu, B. Huang

Department of Materials Science and Engineering  
Southern University of Science and Technology  
Shenzhen, Guangdong 518055, P. R. China

L. Yuan, Z. Yu  
State Key Laboratory of Materials-oriented Chemical Engineering, College of Chemical Engineering  
Nanjing Tech University  
30 Puzhu South Road, Nanjing 211816, P. R. China

W. Liu

Department of Geriatric Dentistry  
Peking University School and Hospital of Stomatology  
Beijing 100081, P. R. China

 The ORCID identification number(s) for the author(s) of this article can be found under <https://doi.org/10.1002/adfm.202510353>

DOI: 10.1002/adfm.202510353

patient recovery through electrical stimulation. However, current electrical stimulation for wound management relies on portable batteries and tethered connection with the electrically conducting sutures, which are also facing some compelling disadvantages. For example, reliance on portable battery increases the burden of cumbersome equipment and patients' discomforts; while reliance on physical tethering may increase the risk of irritation, inflammation, or infection, especially for those internal wounds.<sup>[10,13]</sup> While self-powered systems leveraging piezoelectric (i.e., P(VDF-TrFE)) or triboelectric materials (i.e., ZnO nanowires) generate ES from biomechanical motion,<sup>[3,14]</sup> their efficacy is limited by motion-dependent output variability and poor spatiotemporal control.<sup>[15,16]</sup> Thus, delivering electrical stimulation in a non-tethered, controlled manner is essential for maximizing therapeutic benefits while mitigating potential risks, highlighting the need for further exploration and development.

In this study, we present a multifunctional magnetoelectric suture (ME suture) platform that enables spatiotemporally-controlled electrical stimulation via non-invasive magnetic field modulation for advanced wound management (**Figure 1a**). The suture architecture integrates three synergistic components: 1) a magnetoelectric composite fiber comprising cobalt ferrite-barium titanate core-shell nanoparticles (CFO@BTO NPs) embedded in a piezoelectric P(VDF-TrFE) matrix; 2) a tissue-adaptive polyzwitterionic hydrogel coating (poly(2-(methacryloyloxy)ethyl)dimethyl-(3-sulfopropyl) ammonium hydroxide, PDMAPS), and 3) a magneto-mechano-electric transduction mechanism that converts external magnetic fields into tunable electrical outputs (30–50 mV). The CFO@BTO/P(VDF-TrFE) core exhibits cascaded energy conversion, where magnetic field-induced mechanical deformation of the piezoelectric polymer generates sustained interfacial electric potentials, bypassing the need for wired power sources or implanted batteries. Complementing this, the PDMAPS hydrogel skin serves a dual role: its modulus-matching capability minimizes stress concentration at the tissue-suture interface, while its antifouling character reduces fibrous encapsulation and inflammatory responses (**Figure 1b–d**). This design addresses critical limitations of conventional electrical stimulation devices, such as batteries,<sup>[17–19]</sup> triboelectric nanogenerator (TENGs),<sup>[2,3,16,20]</sup> piezoelectric generators (PEGs)<sup>[16,21–23]</sup> and wireless energy supply,<sup>[24–27]</sup> by combining wireless programmability with biomechanical compliance akin to biological tissues (**Figure 1e**). Furthermore, the hydrogel's ultralow friction coefficient facilitates atraumatic suture removal, enhancing patient comfort and reducing tissue damage. By unifying magnetoelectrically driven bioactivation, inflammation-suppressing interfaces, and dynamic stress redistribution, this platform represents a paradigm shift in intelligent wound management, with translational potential for personalized tissue regeneration strategies.

## 2. Results and Discussion

### 2.1. Design and Fabrication of the ME Sutures

We developed sutures by using a piezoelectric polymer P(VDF-TrFE) as the fiber substrate, while incorporation of magnetoelectric nanoparticles (CFO@BTO NPs) within the polymer matrix could impart the ME sutures with distinct magnetoelec-

tric performances. As schematically illustrated in **Figure S1** and **Movie S1** (Supporting Information), the ME sutures were fabricated through a wet-spinning process. Specifically, 4 wt.% of CFO@BTO NPs (diameter of 40 nm, **Figure S2**, Supporting Information) were dispersed in a 40 wt.% P(VDF-TrFE)/DMSO solution, followed by wet-spinning with water/EtOH (90/10 vol.%) as the coagulation bath. Phase change during the solvent exchange induced the immediate gelation for fiber fabrication. This process allows for scalable production of kilometer-long sutures with uniform diameters ranging from 100 to 800  $\mu\text{m}$ , by tailoring the nozzle size and extrusion ratio, making them suitable for a variety of suturing applications (**Figure 1d**; **Figure S3**, Supporting Information). For example, 4-0 or 2-0 sutures (diameter of 150 to 300  $\mu\text{m}$ ) are used for closing muscles and skin, while 4-0 to 6-0 sutures (diameter of 70 to 200  $\mu\text{m}$ ) are typically applied to seal internal organs such as blood vessels and the gastrointestinal tracts.<sup>[28,29]</sup> The ME suture exhibited a porous structure due to the solvent exchange process (**Figure S4**, Supporting Information), which can impair the electrical output of P(VDF-TrFE) compared to a solid structure.<sup>[30]</sup> The ME sutures were then subjected to high-voltage polarization to align the PVDF electric domains, imparting the fibers with distinct piezoelectric properties, as evidenced by the increase of  $d_{33}$  coefficient from 0.4 to 4 pC/N (**Figure S5**, Supporting Information). Additionally, a polyzwitterionic hydrogel skin (thickness of  $\approx$ 20  $\mu\text{m}$ ) was formulated on the ME suture (see more details in the Experimental part), in order to provide a mechanically compliant biointerface and also improved biocompatibility (**Figure S6**, Supporting Information).

### 2.2. Magnetoelectric Performances of the ME Sutures

Magnetostriuctive materials (i.e., CFO@BTO NPs) deform upon exposure to external magnetic fields, altering their length and volume through domain wall movement and rotation (**Figure S7**, Supporting Information).<sup>[31]</sup> For example, once the CFO@BTO NPs are exposed to a 100-mT magnetic field, they experienced a deformation ratio of -13%, 16.5%, and 17% along the X, Y, and Z axes (**Figure S8**, Supporting Information), respectively. Once these CFO@BTO NPs were incorporated within a polymer matrix, for example, piezoelectric P(VDF-TrFE), the mechanical deformation further induced the generation of electrical potentials (**Figure 2a**; **Figures S8–S10**, Supporting Information). This mechanism enables remote electrical stimulation through spatiotemporal magnetic modulation, providing a non-contact way to activate the piezoelectric responses.<sup>[16,31]</sup> The electrical output is determined by the extent of material deformation, which depends on the magnetic field strength rather than its direction. Similarly, electromagnetic induction has gained increasing attention for magnetic field energy conversion, though it is more commonly utilized in applications such as wireless energy harvesting and smart sensing.<sup>[32,33]</sup> As shown in **Figure 2b,c**, the surface potential of the ME suture significantly increased upon exposure to an external magnetic field (100 mT), with a quantitative increase of 400 mV. To further understand how nanoparticle deformation leads to stress propagation and the generation of electrical potential, we used finite element analysis to clarify the mechanism underlying the magnetoelectric coupling effect, with all relevant parameters listed in **Table S2** (Supporting Information).

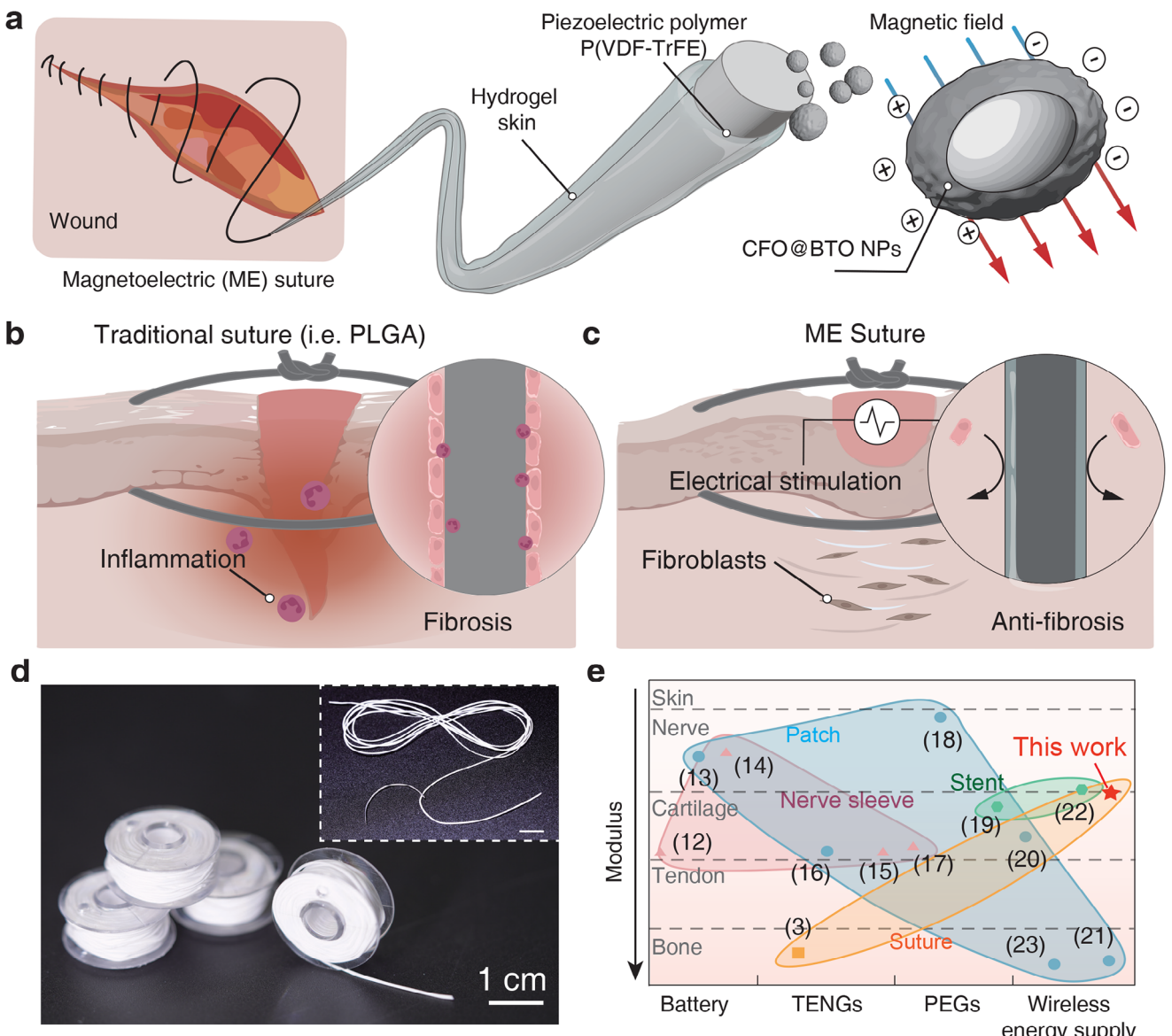


**Figure 1.** | Magnetoelectric fibers as suture (ME suture) for wound management. a) Schematic illustration of wound closure using the ME sutures. The ME sutures are constructed by embedding core-shell magnetoelectric nanoparticles (CFO@BTO NPs) within a P(VDF-TrFE) matrix through wet spinning, followed by functionalizing the fibers with a polyzwitterionic hydrogel skin. b) Schematic illustration of wound closure using traditional sutures (i.e., PLGA or Nylon), which is accompanied with tissue damage, persistent inflammation, and fibrosis formation, in light of the dramatic mechanical mismatch between commercial sutures (i.e., Young's modulus of ca. 2000 MPa for PLGA) with biological tissues (Young's modulus of ca. 100 kPa for the skins). c) ME sutures offer the capability of electrical stimulation for accelerated wound healing through magnetic triggers. Additionally, the outer hydrogel skin exhibits a mechanical compliance (Young's modulus of ca. 70 MPa for our ME sutures) with the biological tissues and lower interfacial friction coefficient, thus mitigating the inflammatory response. d) Representative image of the ME sutures (diameter of approximately 200  $\mu\text{m}$ ) through scalable production, and it could integrated with suture needle for clinical stitching. Scale bar: 1 cm. e) Comparison chart illustrating the mechanical compliance of our ME sutures compared to previously reported electrical stimulation devices for wound management. Data for the Young's modulus were adapted from previously reported literatures, including the battery,<sup>[17–19]</sup> triboelectric nanogenerator (TENGs),<sup>[2,3,16,20]</sup> piezoelectric generators (PEGs),<sup>[16,21–23]</sup> and wireless energy supplies,<sup>[24–27]</sup> with detailed information provided in Table S1 (Supporting Information).

As shown in Figure S9 (Supporting Information), stress distribution within the CFO core increased notably as the magnetic field intensity increased from 0 mT to 200 mT. Similarly, the polarization level of the BTO shell and the surface potential of the P(VDF-TrFE) matrix both increased from 0 to 100 mV and from 0 to 600 mV, respectively, is consistent with our AFM tests (Figure S10,

Supporting Information). It is important to emphasize that the magnetoelectric voltage coupling mechanism operates based on the principle of the piezoelectric effect. Under a static magnetic field, only a single deformation of the CFO@BTO nanoparticles is induced, leading to a one-time pressure generation and a corresponding electrical release. No additional voltage is generated,

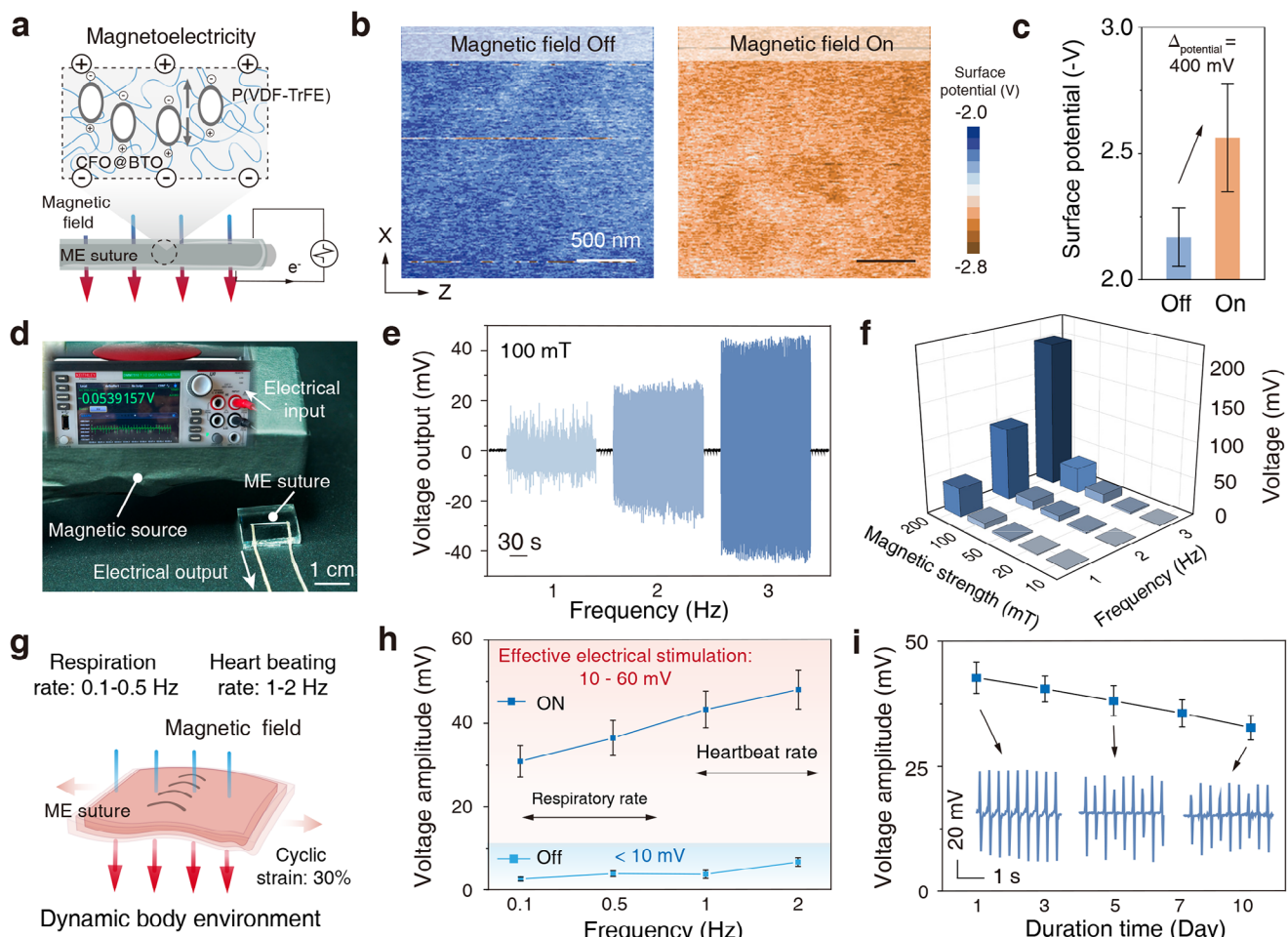


**Figure 2.** | Magnetoelectric properties of the ME sutures. a) Schematic illustration of the underlying mechanism for electrical discharge for the ME sutures. Upon exposure to a magnetic field, the magnetostriuctive CFO@BTO NPs experience mechanical deformation, which further generates mechanical stress and exert onto the P(VDF-TrFE), thus inducing the piezoelectric effect. b) KPFM images recording surface potentials for the ME films ( $\approx 40 \mu\text{m}$  thickness, CFO@BTO NPs fraction of 10 wt.%) in the presence and absence of a magnetic field (100 mT). c) Summary of the surface potential with magnetic field On or Off. d) Experimental setup for quantifying the electrical output for ME sutures activated by an external magnetic field. e) Output voltage traces for the ME sutures upon exposure to a 100-mT magnetic field of various frequencies (1, 2, and 3 Hz). f) Plotting output voltage against magnetic field strengths (10, 20, 50, 100, and 200 mT) and frequencies (1, 2, and 3 Hz). g) Schematic diagram of electrical discharge for the ME sutures in the frequencies of physiological activities, including body movement, respiration, and heartbeat, when the ME suture is stitched within a biological tissue. h) Plotting of voltage amplitude against the frequencies within the range of physiological activities (0.1–2 Hz). The magnetic field is set as 100 mT and 3 Hz, while a cyclic mechanical strain for the biological tissue is set at 30%. i) Evolution of voltage amplitude for the ME suture, which is stitched within porcine skin, during a 10-day storage. The ME sample was exposed to magnetic trigger (100 mT and 3 Hz) for one hour per day. The inset displays the output voltage signals on Day 1, 3, and 10, respectively. Data in (c), (h), and (i) are presented as means  $\pm$  S.D.,  $n = 3$ .

and the charge gradually returns to its initial state (Figure S11, Supporting Information). These results suggest that the magnetoelectric coupling in our ME suture presents a promising solution for electrical stimulation through magnetoelectric modulation.

To quantify the magnetoelectric performance of our ME sutures, we encapsulated a 200- $\mu\text{m}$  ME suture sample (corresponding to 3–0 suture) within PDMS, and the magnetic field-induced electric output was recorded (Figure 2d; Movie S2, Supporting Information). The PDMS encapsulation provides electrical insulation, preventing signal leakage, and shielding the material from external electromagnetic interference, ensuring continuous generation of electrical signals. The magnetic field strength, in the

range of 10 to 200 mT, could be varied by tuning the distance between a permanent magnet and the ME suture from 2 to 50 mm, resulting in output voltage up to 200 mV (Figure 2e–f; Figure S12, Supporting Information). Additionally, the output voltage could also be tailored by tuning the frequency of the magnetic field. A higher frequency is accompanied by periodical mechanical deformation of CFO@BTO NPs, which accordingly accelerates both charge accumulation and release of the piezoelectric P(VDF-TrFE) substrate.<sup>[34]</sup> As shown in Figure 2e, with the frequency increasing from 1 to 3 Hz with a fixed 100-mT magnetic field, the output voltage increased from 10 to 40 mV. At low magnetic field frequencies, such as 1 Hz, the overall electrical output decreases, making signal noise more pronounced. As reported by previous

studies,<sup>[12]</sup> electrical stimulation at a voltage of ca. 40 mV was widely used for wound healing, since this voltage approaches the trans-epithelial potential of wound tissue (10–60 mV). As illustrated in Figure S12 (Supporting Information), when the magnetic source is positioned at a distance of 2 mm, the magnetic field strength reaches 200 mT. This magnetic loading at 1 Hz generates an output voltage of 40–50 mV, enabling effective electrical stimulation. However, the low distance between the magnet and the suture increases the risk of direct contact due to physiological activity (e.g., breathing and hearting), which may lead to device malfunction or tissue damage. Here, we chose a magnetic field of 100 mT, a frequency of 3 Hz, and a 10-mm distance between the permanent magnet and the ME sutures for further electrical stimulation at 40 mV. Moreover, we investigated the effects of different temperatures (25, 37, and 50 °C) and physiological fluid environments on the electrical output. The results demonstrate that our ME sutures can continuously generate electrical signals under physiological conditions, including body temperature and biological fluids, with an electrical output sufficient to compensate the endogenous wound electric field (10 – 860 mV, Figure S13, Supporting Information).

The electrical performance of the ME suture under dynamic conditions was also assessed by measuring the output voltage within the frequency range of respiration and heart beating scenarios (0.1–2 Hz). As illustrated in Figure 2g–h and Figure S14 (Supporting Information), when the ME suture experienced cyclic deformation at a strain of 30% (average strain for biological skins),<sup>[35]</sup> despite the absence of magnetic field, it was also accompanied with a moderate voltage output below 10 mV, attributing to the piezoelectric response of P(VDF-TrFE). However, upon exposure to an external magnetic field (100 mT, 3 Hz), the output voltage increased significantly by 6–8 times, highlighting the crucial role of magnetic field in magnetoelectric response of our ME sutures. To assess the ME suture's stability in magnetoelectric response, the samples were periodically subjected to magnetic field over a 10-day period (Figure 2i). The output voltage experienced a slight decrease from 42 to 32 mV, however, remained above 10 mV, which is sufficient to offer electrical modulation for wound management. This sustainable electrical output over a period of 10 days corresponds well with the typical wound healing period of 7–10 days before suture removal.<sup>[36]</sup>

### 2.3. Mechanical Compliance of the ME Sutures

The efficacy of surgical sutures depends on their capability to endure the dynamic strain (skin strain: 20%–40%) and stress (bulk tissues: 0.8–1.2 MPa) exerted on the sutures throughout the whole healing process,<sup>[35,39,40]</sup> which underscores the importance of mechanical strength. Commercial sutures are made from rigid polymers, like nylon and PLGA, with Young's modulus exceeding 1 GPa, which can provide adequate sealing strength during the wound repairing.<sup>[1]</sup> However, the strike mechanical mismatch between polymer sutures and biological tissues (Young's modulus  $\approx$  100 kPa) can result in numerous side effects, including tissue damage, inflammation, and also deteriorated healing efficacy. Moreover, the rough surfaces of sutures, particularly braided ones, can increase friction against surrounding tissues during the stitching and suture removal processes.<sup>[1]</sup>

In our case, the introduction of polyzwitterionic hydrogel skin offers a mechanically compliant and antifouling biointerface (Figure S6, Supporting Information), which could reduce the friction against tissues during suture movement, thereby minimizing inflammation and enabling an improved healing outcome.

As depicted in Figure S15 (Supporting Information), the ME suture (diameter of 200  $\mu\text{m}$ ) with polyzwitterionic hydrogel skin can sustain a maximal strain of 180% and strength of 25 MPa. We then evaluated the stress resistance of our ME sutures in the stitched porcine skin to mimic the body movement at a maximal strain of 30% (Movie S3 and Figure S16–S17, Supporting Information). For the stitched joint with ME suture, the maximal force reached 0.45 N, which was 28% lower than that of 3-0 PLGA sutures (Figure 3a,b), indicating that mechanical properties of the ME sutures are adequate for effective wound closure. Moreover, the stitched pinholes in the PLGA groups were 2.2-fold larger in area than those in the ME suture group at the same strain (Figure 3c). This difference could be ascribed to the higher mechanical modulus of PLGA, accompanied by increased stress concentration in tissues near the pinholes during stretching. To validate our hypothesis, we developed a finite element model (FEM) in ABAQUS to simulate the stress distribution at the sutured wound sites under mechanical loading. It is shown that the ME suture generated substantially lower stress around stitched pinholes, which was up to 60x lower than that of PLGA sutures (Figure 3d–h). For rigid polymer sutures like PLGA, such high stress concentration around the stitched pinholes is inevitable under dynamic biological motion, accompanied by continuous tissue damage, thus impeding the wound healing. In contrast, our ME suture effectively mitigated local stress concentration, fostering a mechanically compliant microenvironment, thus mitigating the inflammatory response and accelerating tissue regeneration.

We further conducted nanoindentation tests to compare the hardness and reduced modulus of the ME sutures and the PLGA sutures (Figures S18–S19, Supporting Information). The ME sutures exhibited relatively lower hardness and reduced modulus, which are 29-fold and 60-fold lower than the PLGA sutures, respectively. This further explained how our suture effectively mitigate stress concentration in light of the compliance in mechanics. In Figure 3e and Table S3 (Supporting Information), we compared the mechanical compliance, the modulus matching factors (MMF) that are defined as the ratio of the suture modulus to the tissue modulus, together with previously reported functional sutures, including commercially PLGA, conducting composite fibers, and biologically functionalized sutures.<sup>[2–6,37,38]</sup> Most of those functionalized sutures, designed to provide adequate strength for wound healing, exhibit Young's moduli of 0.5 to 15 GPa and are comparable to those of commercial sutures. However, their mechanical compatibility factors (MMF), located in the range of 1,000 to 40,000, are typically over two orders of magnitude higher than that of our ME suture (MMF: 175). For instance, for electron conducting suture functionalized with the conductive polymer poly(3,4-ethylenedioxythiophene)-poly(styrene sulfonate) (PEDOT:PSS), it has been proven capable to detect leakage in gastrointestinal anastomosis.<sup>[4]</sup> Even though the high tissue compatibility factor (MMF: 4400) enables the mechanical support, it may also cause tissue damage and stress

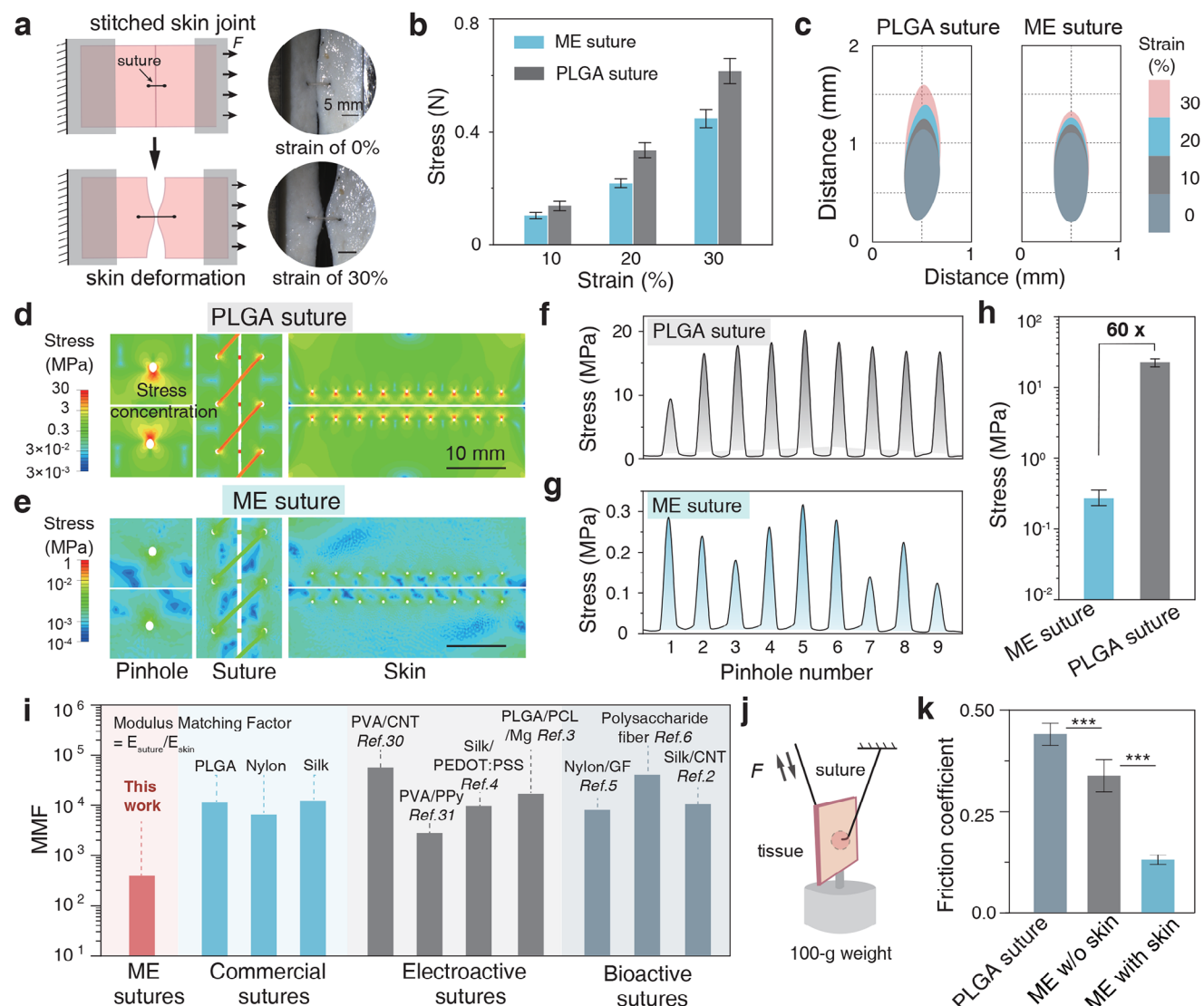


**Figure 3.** | Mechanical compliance of the ME sutures. a) Schematic illustration and images of a porcine skin joint stitched with ME or PLGA sutures before and after being stretched to a strain of 30%. b) Force measured upon being stretched to a strain of 10%, 20%, and 30% for the stitched joints. c) Deformation of the stitched pinholes on the porcine skin at a strain of 10%, 20%, and 30%. d,e) Finite element analysis (FEA) simulating the stress distribution for wounds stitched with PLGA (d) or our ME (e) sutures at a strain of 5%. f-g) Evolution of the stress along the stitched pinholes for both PLGA (f) or our ME (g) sutures. h) Summary of the maximal stress at the stitched pinholes for both PLGA and our ME sutures. i) Comparison of modulus matching factors (MMF) for our ME sutures, commercial sutures (i.e., PLGA, nylon and silk), and previously reported sutures (e.g., electroactive sutures,<sup>[3,4,37,38]</sup> antibacterial sutures,<sup>[2]</sup> and drug-delivery sutures),<sup>[5,6]</sup> while all the data were adapted from these literatures. j) Experimental setup for quantifying the friction coefficient. k) Summary of the measured friction coefficients for ME sutures with or without hydrogel skin, and also commercial PLGA sutures. Data in (b) and (k) are presented as means  $\pm$  S.D.,  $n = 3$ . Data points in (h) are averaged from the maximal stress of nine pinholes.

concentration, thereby potentially increasing the risk of anastomotic leakage.

In addition to its superior mechanical compatibility, our ME sutures are also functionalized with a polyzwitterionic hydrogel skin, offering a smooth coating that significantly reduces the interfacial friction coefficient against biological tissues, as well as antifouling performance. As shown in Figure 3j and Figure S20 (Supporting Information), the ME sutures with hydrogel skin displayed a significantly lower friction coefficient (0.13) compared to both the ME suture without hydrogel skin (0.34) and the PLGA suture (0.45) during ex vivo friction tests against porcine skins.

Notably, this lower friction coefficient was also observed in other tissues and organs (e.g., tendons and intestines), highlighting the potential of ME sutures for various *in vivo* wound sealing through suturing. To further evaluate the antifouling properties, we immersed the ME suture in fluorescein isothiocyanate-tagged bovine serum albumin (FITC-BSA, 1 mg mL<sup>-1</sup>) solution, simulating an *in vivo* biofluidic environments (Figure S21, Supporting Information). Confocal laser scanning microscopic (CLSM) images evidenced no observable protein absorption on the ME suture with hydrogel skin (Figure S20d,e, Supporting Information). In contrast, the PLGA and ME suture without hydrogel skin

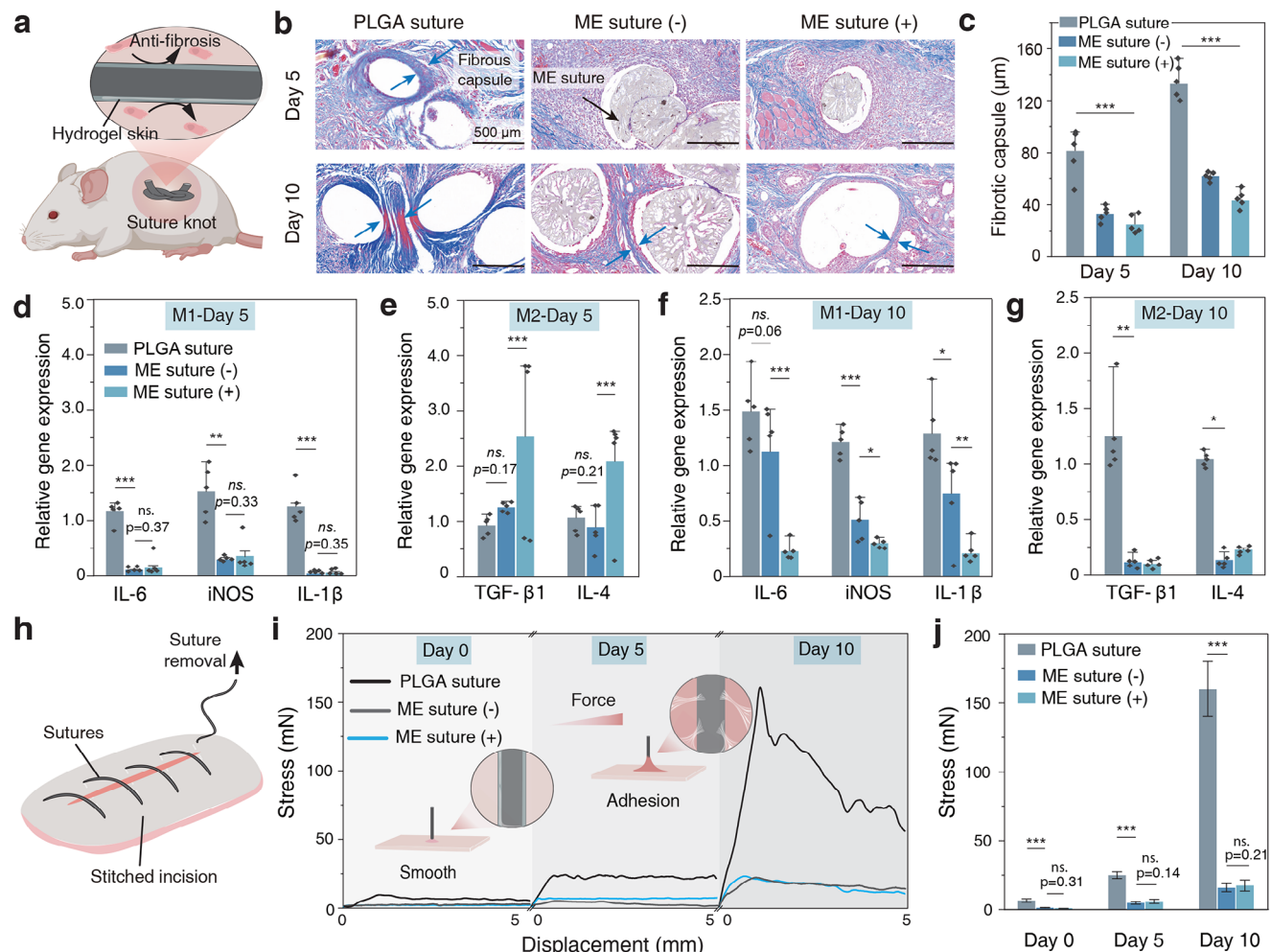


**Figure 4.** | Biocompatible and antifouling ME suture-tissue interface. a) Illustrated depiction of the subcutaneous implantation of ME suture knots within a rat model, and the antifibrosis mechanism for the polyzwitterionic hydrogel skin, which effectively prevents foulant adsorption and collagen deposition. b) Representative Masson's trichrome staining images of tissue containing sutures after 5- and 10-day subcutaneous implantation for different groups, ME sutures with or without hydrogel skin, and commercial PLGA sutures. Scale bar: 500 µm. c) Thickness of the fibrotic capsule formed around the implanted sutures during the subcutaneous implantation. d–g) Relative gene expression of inflammatory markers at the suture-tissue interface, collected on Day 5 (d–e) and Day 10 (f–g) post-implantation at the subcutaneous dorsal site. The data were normalized to the corresponding PLGA group for each time point using original qPCR results. h) Illustrated depiction of the suture removal after wound healing. i–j) Force measurements (i) and statistical maximal force (j) during the suture removal from rat tissues at 5-day and 10-day post-wound healing. Data are presented as means ± S.D. ( $n = 5$ ). Statistical significance and  $p$  values were determined by two-sided unpaired  $t$ -tests; ns, not significant; \* $p < 0.05$ , \*\* $p < 0.01$ , \*\*\* $p < 0.001$ .

showed bright green fluorescence, with protein adsorption levels 30× and 35× higher than with hydrogel skins, respectively.

#### 2.4. Biocompatibility and Antifibrosis of the ME Sutures

We then tested the biocompatibility of the ME sutures, both with and without the hydrogel skin, using NIH3T3 cell cultures. Both qualitative and quantitative cell analysis evidenced the superior in vitro cytocompatibility of our ME suture samples during a 5-day cell culture (Figure S22, Supporting Information). The superior biosafety of the ME suture can be attributed to the incorporation of CFO@BTO NPs into the P(VDF-TrFE) matrix during the solvent exchange process. Additionally, a hydrogel skin shell was fabricated on the surface of the P(VDF-TrFE) to further

prevent nanoparticle leakage. To further evaluate the inflammatory response and fibrous capsule formation over time, ME suture knots were subcutaneously implanted in the dorsal pockets of rats (Figure 4a,  $n = 10$ ) and then exposed to magnetic field (ME suture (+)), while implanted ME sutures without magnetic treatment (ME suture (-)) and commercial PLGA sutures (3–0) were tested as controls. Upon 5-day post-implantation, the ME suture (+) exhibited a significantly thinner fibrous capsule ( $25 \pm 7 \mu\text{m}$ ), compared to the PLGA suture layers ( $80 \pm 17 \mu\text{m}$ ) (Figure 4b,c). Rigid essence and rough surface of PLGA suture may induce sustained friction against the surrounding tissue during daily physiological movement, which is always accompanied with tissue damage, excessive inflammation, over-expression of collagen, and subsequent fibrosis.<sup>[18]</sup> In contrast, the ME(-) group showed no significant difference in fibrous capsule formation

( $33 \pm 6 \mu\text{m}$ ), due to its mechanical compliance and antifouling properties of the polyzwitterionic hydrogel skin during the 5-day implantation.

Macrophages, as tissue-resident innate immune cells, are crucial in the initiation, regulation, and resolution of inflammation, with two key subtypes: pro-inflammatory (M1) and anti-inflammatory (M2) macrophages.<sup>[18,41]</sup> According to the qPCR analysis (Figure 4d,e), the ME suture (+) group showed significantly lower expression of pro-inflammatory cytokines (IL-6, iNOS, and IL-1 $\beta$ ) on Day 5 compared to the PLGA suture group. Quantitatively, IL-6, iNOS, and IL-1 $\beta$  expression levels in the ME suture (+) group were down-regulated by 88%, 77%, and 96%, respectively. In addition, the ME suture (+) exhibited higher levels of anti-inflammatory cytokines (TGF- $\beta$ 1 and IL-4), which were elevated by 100% and 132% compared to the ME suture (-) group on Day 5 post-implantation. This suggests that electrical stimulation with ME suture (+) accelerated the inflammatory phase at the suture-tissue interface. It is noteworthy that the PLGA suture group maintained significantly elevated levels of both pro-inflammatory and anti-inflammatory cytokines throughout the 10-day implantation, with TGF- $\beta$ 1 expression being 10-fold and 12-fold higher than in the ME suture (-) and ME suture (+) groups, respectively. Prolonged exposure to high levels of TGF- $\beta$ 1 is known to induce myofibroblast activation and persistent fibrosis,<sup>[42]</sup> and we attribute this sustained inflammatory response in the PLGA sutures to tissue damage caused by repeated friction at the suture-tissue interface.

Thanks to the outstanding properties of our ME sutures, such as antifouling capability, inflammation reduction, and minimized fibrotic encapsulation, our ME sutures not only provide effective wound closure but also greatly improve the compliance of suture removal by reducing tissue damage and alleviating discomfort. The frictional force during suture removal was quantified by pulling the suture through rat skin at a constant speed ( $0.5 \text{ mm s}^{-1}$ ) after 0, 5, and 10-day stitching (Figure 4h-j; Figure S23, Supporting Information). In the PLGA suture group, the maximum friction force increased significantly by 24-fold after 10-day stitching treatment, in consistence with the observed increase in fibrotic encapsulation thickness (Figure 4b,c). In contrast, the ME sutures with an antifouling hydrogel surface showed a significant reduction in friction force by a factor of ten compared to the PLGA group (Figure 4j), thus enabling a benign suture removal and mitigated patients' discomfort. Even though there is growing interest in developing absorbable sutures, which could effectively avoid the necessity of suture removal. However, absorbable sutures are commonly used in internal and cosmetic surgeries, facing risks arising from premature degradation, potentially leading to wound closure failure. For suturing tissues that require high mechanical strength, such as Achilles tendon repairing or gastrointestinal anastomosis, early suture degradation can cause severe complications. Consequently, non-absorbable sutures are often preferred for their reliability and improved postoperative outcomes. In contrast, our ME sutures show great promise, particularly for applications requiring the suturing of mechanically active tissues, not to mention that it provides essential mechanical support, reduces stress concentration, and improves the compliance of suture removal.

## 2.5. ME Suture for Wound Management in Rat Model

After verifying the ME sutures' magnetoelectric performance, mechanical compatibility, and in vivo antifouling properties, we further evaluated its efficacy in wound management. A full-thickness dorsal skin incision ( $\approx 2 \text{ cm}$ ) was made on a Sprague-Dawley rat model (male, 250–300 g) and stitched with our ME sutures, and then exposed to a magnetic field (100 mT, 3 Hz) for one hour per day (termed as ME suture (+)). Control groups, including ME sutures without magnetic treatment (ME suture (-)) and commercial 3-0 PLGA sutures ( $n = 10$ ; Figure 5a; Figure S24 and Movie S4, Supporting Information), were conducted for comparison. As shown in Figure 5b, the ME suture (+) group achieved a wound healing effect on Day 5 comparable to that of PLGA group at Day 10, the gold standard timeline for suture removal. Further H&E staining imaging disclosed severe tissue swelling and deformation for the PLGA group, accompanying with a fivefold increase in inflammatory cell appearance compared to the ME sutures on Day 5 (Figure 5c; Figure S24, Supporting Information), arising from the mechanical mismatch between the PLGA and biological tissues. Additionally, a persistent inflammatory response, 2.0-fold compared to ME suture (+), was observed in the tissue surrounding PLGA sutures up to 10 days post-treatment, suggesting that the high modulus of PLGA sutures induces tissue trauma during body movement, resulting in chronic inflammation (Figure S25, Supporting Information).

Electrical stimulation has been proven effective in accelerating wound healing by enhancing cell proliferation, migration, and extracellular matrix deposition.<sup>[10,13]</sup> The ME sutures can readily provide effective electrical stimulation (30–50 mV) through the magnetoelectric effects, thus promoting wound repair. We then conducted immunofluorescent analysis on the repaired tissues by evaluating the expression of the tumor suppressor phosphatase and tensin homolog (Pten, Figure 5d-e), a mediator for directional cell migration in response to electrical signals.<sup>[12]</sup> The ME suture (+) group exhibited significantly higher levels of Pten+ cells ( $84\% \pm 5\%$ ) on Day 5, compared to the ME suture (-) group ( $46\% \pm 12\%$ ). This result suggests that effective electrical stimulation was produced in the ME suture group following exposure to magnetic field treatment. Interestingly, the expression of Pten remained elevated in the electrotactic keratinocytes within the ME (+) group's repairing tissues compared to both the ME (-) and PLGA groups, extending up to 10 days post-treatment. The electric field generated by the ME suture (+) provides directional cues for cell migration, with keratinocytes responding to voltages as low as  $10\text{--}25 \text{ mV mm}^{-1}$ .<sup>[12]</sup> The electric field induces polarity changes in keratinocytes, leading to the aggregation of surface receptors (e.g., EGFR) and ion channels (e.g.,  $\text{Ca}^{2+}$  channels) on the side exposed to the field.<sup>[43]</sup> This promotes the migration of keratinocytes toward the wound, thereby enhancing wound healing. As depicted as Figure 5f,g, immunohistochemical analysis of keratin 14 (Krt14), a marker for undifferentiated keratinocytes, revealed re-epithelialization rates of  $85\% \pm 33\%$  in the PLGA suture group at Day 10, while the ME suture (+) group showed  $95\% \pm 0.7\%$  re-epithelialization after just 5 days of treatment, with the wound nearly closed. Notably, the re-epithelialization rate in the ME suture (+) group was 17% higher at Day 5 compared to the ME suture (-) group ( $81\% \pm 5\%$ ), suggesting that electrical stimulation in the ME suture

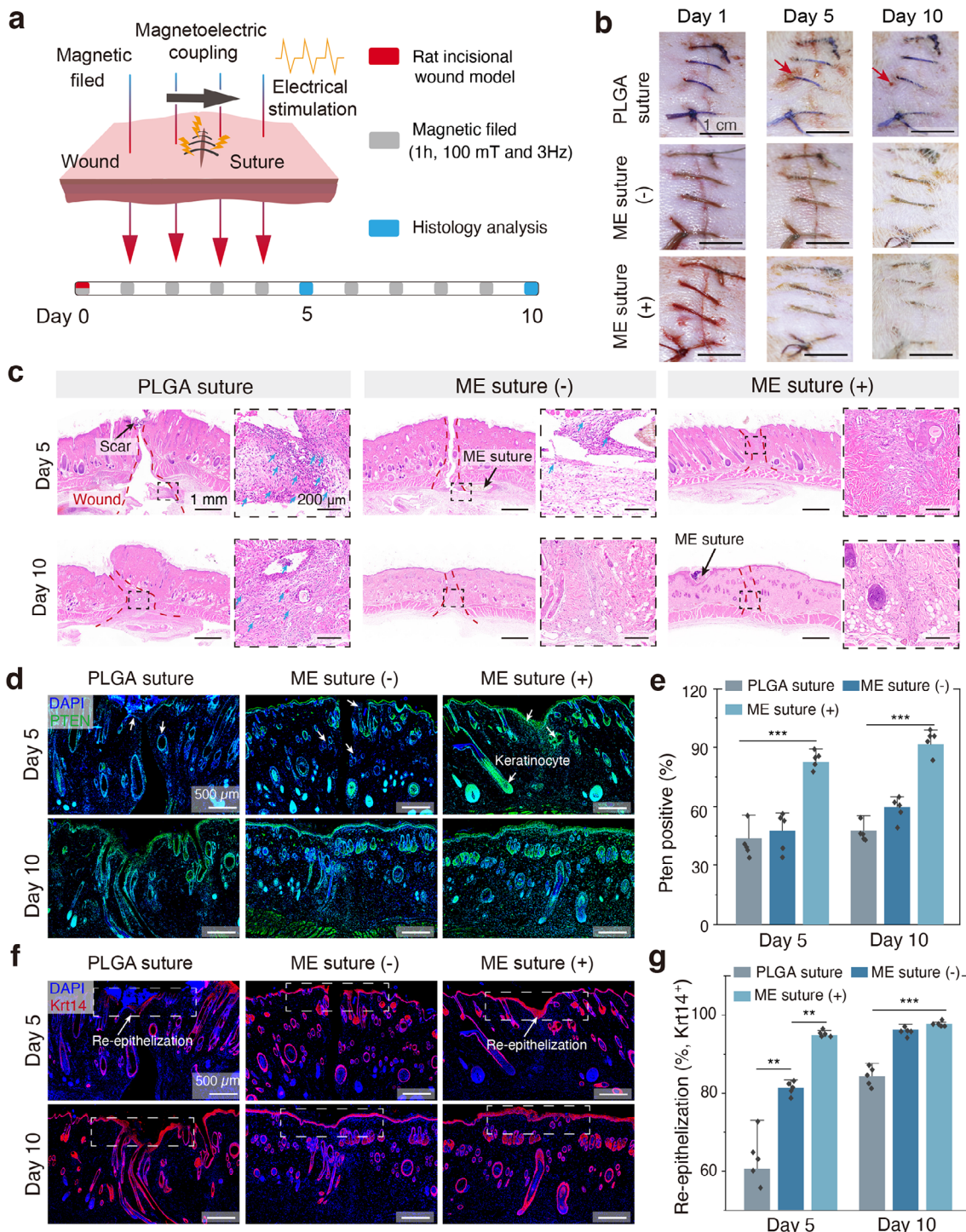


**Figure 5.** | ME sutures for magnetic field-mediated wound management. a) Schematic illustration of incision wounds stitched with ME sutures. A magnetic field is applied one hour per day, in order to induce the electrical discharge for accelerated wound healing. b) Representative images recording the 10-day wound healing, which are sutured with ME sutures or commercial PLGA 3-0 sutures. ME sutures without magnetic field were tested as a control. Scale bar: 1 cm. c) Representative hematoxylin and eosin (HE) staining images of wound tissues at Day 5 and Day 10 for three different groups. Scale bar: 1 mm. The black dashed boxes represent a 7× magnified images of the HE staining images, and blue arrows for inflammatory cells. Scale bar: 200 μm. d,e) Representative immunofluorescent staining images for phosphatase and tensin homolog (Pten, green fluorescence, d), and quantitative analysis of relative positive areas of Pten (e) at 5- and 10-day treatment. Scale bar: 500 μm. f-g) Representative immunofluorescent staining images for keratin 14 (Krt14) (green fluorescence, f), and quantitative analysis of relative positive area of Krt14 (g) at 5- and 10-day treatment. Scale bar: 500 μm. Data are presented as means ± S.D. ( $n = 5$ ). Statistical significance and  $p$  values were determined by two-sided unpaired  $t$ -tests; ns, not significant; \* $p < 0.05$ , \*\* $p < 0.01$ , \*\*\* $p < 0.001$ .

(+) group effectively promotes wound healing. Collectively, these findings confirm that ME sutures provide mechanical compatibilities to mitigate inflammation responses, and also electrical stimulation to promote cell proliferation and keratinocyte migration through the magnetoelectric effect, thereby significantly accelerating wound healing. It is deserved to mention that, the repairing efficacy of the ME suture (+) group at Day 5 is comparable to gold-standard 10-day stitching with PLGA suture, thus half time is needed prior to suture removal.

### 3. Conclusion

In summary, we developed a ME suture integrating a mechanically compliant hydrogel interface with wireless electrical stimulation capabilities through magnetic modulation. The ME suture demonstrates efficient magnetoelectric coupling, tunable voltage outputs (30–50 mV), and exceptional mechanical compliance that aligns with biological tissues. Experimental and finite element modelling analyses confirm its dual capacity to withstand dynamic wound stresses while mitigating tissue-level stress concentration. In vivo evaluations using a rat incisional model revealed a 50% reduction in healing time compared to commercial PLGA sutures (5 vs. 10 days), attributed to suppressed inflammatory responses, minimized tissue deformation, and electrical stimulation-enhanced cellular proliferation. This technology also establishes a scalable framework for multifunctional sutures that could synergize wound closure with sensing or monitoring through modular integration.

Future efforts will prioritize translating this platform to clinical applications, addressing key challenges such as designing wearable or localized magnetic field delivery systems to ensure patient compliance and therapeutic precision. Critical next steps include optimizing suture mechanical properties, defining magnetic stimulation parameters tailored to human anatomical regions, and conducting preclinical studies to evaluate interspecies variations in immune responses and tissue regeneration. These investigations are also essential to bridge the gap between rodent models and human physiology, particularly regarding tissue composition, biomechanical demands, and long-term biocompatibility. By resolving these challenges, ME sutures may evolve into a versatile bioelectronic toolkit for advanced wound management.

### 4. Experimental Section

**Preparation of ME Suture:** 0.4 g CFO@BTO core-shell NPs were dispersed in DMSO (10 mL) under 1-h ultrasonication (540 W, 40 kHz), followed by adding P(VDF-TrFE) powders (4 g) under 1-h stirring (600 rpm). The mixture was transferred into a syringe and pneumatically extruded into an ethanol/water solution (10/90 vol.%) at a pressure of 0.6 MPa. The crude fibers were soaked into deionized water for 12 h for further solidification, and then dried at 60 °C for 12 h, followed by another 90-min thermal annealing at 120 °C. The as-obtained CFO@BTO/P(VDF-TrFE) fiber samples were further polarized with a corona poling in a DC electric field of 10 kV for 30 min at room temperature.

To introduce the hydrogel skin, these crude fibers were treated with plasma (PDC-001, Harrick Plasma) for 3 min, and then soaked with in a benzophenone/ethanol solution (10 wt.%) for 5 min. After drying under nitrogen flow, the substrates were immersed into a monomer precursor solution, which was consisted of 50 wt.% 2-(methacryloyloxy)ethyl]dimethyl-

(3-sulfopropyl)ammonium hydroxide (DMAPS) and 5 wt.%  $\alpha$ -ketoglutaric acid. After 120-min UV curing (365 nm, 20 mWcm<sup>-2</sup>), the fiber samples were then thoroughly rinsed with excessive amount of deionized water for 120 h, in order to remove the unreacted residues, followed by drying under nitrogen flow, resulting in the final ME sutures.

**Magnetic Field Triggered Electrical Stimulation:** The magnetic stimulation equipment was manually assembled with a stirring apparatus (rate up to 180 rpm) and strong magnets (maximal strength of 200 mT), as shown in Figure S12 (Supporting Information). The suture test unit was composed of stitches, conductive copper tape and PDMS package. By tuning the distance between the magnet and the suture sample, the magnetic field intensity was gradually changed from 10 to 200 mT, and the magnetic field cutting frequency was regulated by changing the rotation speed from 60 to 180 rpm (1 to 3 Hz).

The ME suture was encapsulated within PDMS matrix with electrodes, and then connected to the positive and negative electrodes of an oscilloscope to record the instantaneous voltage intensity, while the ME suture sample was loaded on a tensile tester (Cellscale, Canada). A cyclic stretching was applied to the ME suture sample at a strain of 30% and frequency of 0.1–2 Hz, mimicking the daily human activities. To investigate potential interference of this electric signal on the suture's magnetoelectric performance, a magnetic field of 3 Hz and 100 mT was applied simultaneously during pulling, and the electric signal was recorded. Additionally, the long-term stability of the magnetoelectric performance was examined by testing its electrical output under a 3 Hz, 100 mT magnetic field on Day 1, 3, 5, 7, and 10.

**Friction Force and Coefficient Tests:** To probe the damage to skin during the suture removal, the friction force was quantified using a single suture pulling test, as schematically shown in Figure 3a and Figure S15 (Supporting Information). The porcine skin was fixed in a mechanical stretcher (Cellscale), the distance between the two pinholes was set at 5 mm, and the suture was pulled at a speed of 0.5 mms<sup>-1</sup>. The stress during the pulling process was recorded, and stresses at 10%, 20%, and 30% were counted. At the same time, the deformation of the pinhole and the skin edge was recorded by the digital microscope (AM4815ZT, 20 mm pixel<sup>-1</sup>), and the proportion and stress of the deformation were calculated based on the initial stress and deformation (0 MPa and 0%). The distance between the skin edges pulled by the suture was simultaneously recorded.

**Stress Distribution Simulation:** To investigate the effect of suture parameters on stress concentration during skin traction, a 3D finite element model including both the suture and skin was created using ABAQUS software (Dassault Systemes Simulia Corp., RI, USA). In all models, the tissue was modeled as a square with each side measuring 20 mm and a thickness of 0.5 mm. With a distance of 5 mm between two suture holes, the stress-strain field was observed under 0–5% strain. By statistically evaluating the stress around the suture holes, the stress differences between commercial suture models and ME suture models were compared. In all analyses, the commercial suture was treated as a linearly elastic material, while the tissue and ME suture were represented by a hyperelastic constitutive model. For the suture and skin, the neo-Hookean nonlinear constitutive model (incompressible) could be used to describe their mechanical behavior:

$$W = \frac{\mu_i}{2} (C_a : (I - 3)) \quad (1)$$

where  $W$  is the strain energy density function. When  $i = \text{suture}$ ,  $\mu_{\text{suture}}$  represents the shear modulus at risk points; when  $i = \text{skin}$ ,  $\mu_{\text{skin}}$  represents the shear modulus of the skin.  $C_a = A^T A$  is the right Cauchy-Green strain tensor, and  $I$  is the identity tensor.

**Animal Experiments:** All surgical procedures were approved by the Southern University of Science and Technology (SUSTech) Animal Ethics Committee (Protocol Number: SUSTech-JY202402105). The SD rats used in the experiments (Male, 250–300 g) were purchased from Vital River Laboratory Animal Technology Co., Ltd. (Beijing), and were housed and provided veterinary care by trained staff at the Laboratory Animal Center of SUSTech. The ME sutures were sterilized by soaking in 75 v/v% ethanol for 24 h before being used for incisional wound closure.

**In Vivo Biocompatibility Test:** A symmetrical 0.5 cm incision was made in the dorsal subcutaneous tissue, followed by the creation of a small pocket (1 cm) using scissors. The ME suture was tied into a knot and implanted into the subcutaneous pocket, with daily magnetic loading (one hour per day, 100 mT, 3 Hz) applied to activate the electrical stimulation, which was referred to as the ME suture (+). In contrast, a 3-0 commercial PLGA suture and an ME suture without magnetic trigger (designated as the ME suture (-)) were also tested as controls. At designated post-operative time points (Day 5 and Day 10), the implanted sutures and surrounding tissues were excised from the incision sites. Two samples were collected from each rat, one was fixed in 4% paraformaldehyde for 24 h at 4 °C for histological analysis, while the other was soaked in PBS and frozen at -80 °C for subsequent qPCR analysis.

**Incisional Wound Management:** To evaluate the effect of ME sutures on wound closure and healing, a symmetrical 2-cm full-thickness skin incision without tissue loss was created on the lateral dorsum of each rat using a scalpel. Four stitches were placed in the incisional wounds using different types of sutures ( $n = 10$ ). The incision wounds were divided into three treatment groups: ME suture (+), ME suture (-), and PLGA suture. At designated postoperative time points (Day 5 and Day 10), the wounds were photographed, and the healing tissue along with the sutures was collected. Two samples were collected from each rat, one was fixed in 4% paraformaldehyde for 24 h for histological analysis and immunofluorescence staining, while the other was used for quantifying the force required for suture removal.

**Statistical Analysis:** All the data were processed using Origin 2021 and presented as the means  $\pm$  standard deviation (S.D.). One-way analysis of variance (One-way ANOVA) was used to determine the significance level between multiple groups. For statistical analysis between two groups, the two-sided Student's *t*-test was used. The significance levels were considered as \* $p < 0.05$ , \*\* $p < 0.01$ , \*\*\* $p < 0.001$ .

## Supporting Information

Supporting Information is available from the Wiley Online Library or from the author.

## Acknowledgements

Y.Y., P.W., and X.C. contributed equally to this work. The authors acknowledged the financial support by the STI 2030-Major Projects (2022ZD0209500), National Natural Science Foundation of China (52373139, U2436202, and 92366302), Guangdong Basic and Applied Basic Research Foundation (2024A1515240042), Key Talent Recruitment Program of Guangdong Province (2019QN01Y576) and Basic Research Program of Shenzhen (20231116101626002 and JCYJ20240813094159001). The authors also gratefully acknowledged the support from the Shenzhen Science and Technology Innovation Commission (KJZD20240903101400001) and the Development and Reform Commission of Shenzhen Municipality (XMHT20240115003). The authors would also like to acknowledge the technical support from SUSTech Core Research Facilities.

## Conflict of Interest

The authors declare no conflict of interest.

## Data Availability Statement

The data that support the findings of this study are available from the corresponding author upon reasonable request.

Received: April 27, 2025

Published online:

- [1] Z. Ma, Z. Yang, Q. Gao, G. Bao, A. Valiei, F. Yang, R. Huo, C. Wang, G. Song, D. Ma, *Sci. Adv.* **2021**, 7, eabc3012.
- [2] M. Liu, Y. Zhang, K. Liu, G. Zhang, Y. Mao, L. Chen, Y. Peng, T. H. Tao, *Adv. Mater.* **2021**, 33, 2004733.
- [3] Z. Sun, Y. Jin, J. Luo, L. Li, Y. Ding, Y. Luo, Y. Qi, Y. Li, Q. Zhang, K. Li, *Nat. Commun.* **2024**, 15, 8462.
- [4] V. Kalidasan, X. Yang, Z. Xiong, R. R. Li, H. Yao, H. Godaba, S. Obuobi, P. Singh, X. Guan, X. Tian, *Nat. Biomed. Eng.* **2021**, 5, 1217.
- [5] J. Li, S. W. Linderman, C. Zhu, H. Liu, S. Thomopoulos, Y. Xia, *Adv. Mater.* **2016**, 28, 4620.
- [6] M. Do, B. G. Im, J. P. Park, J. H. Jang, H. Lee, *Adv. Funct. Mater.* **2017**, 27, 1702017.
- [7] P. Zhang, Y. Yang, Z. Li, Y. Xue, F. Wang, L. Shan, Y. Wang, X. Shi, K. Wu, J. Liu, *Adv. Funct. Mater.* **2025**, 2422869.
- [8] X. Chen, Y. Feng, P. Zhang, Z. Ni, Y. Xue, J. Liu, *Adv. Mater.* **2024**, 37, 2413476.
- [9] Y. Jiang, A. A. Trotsuk, S. Niu, D. Henn, K. Chen, C.-C. Shih, M. R. Larson, A. M. Mermin-Bunnell, S. Mittal, J.-C. Lai, *Nat. Biotechnol.* **2023**, 41, 652.
- [10] Y. Tan, R. Liao, Y. Mu, L. Dong, X. Chen, Y. Xue, Z. Zheng, F. Wang, Z. Ni, J. Guo, H. Gu, Y. Wang, Z. Wang, L. Zeng, J. Liu, *Adv. Funct. Mater.* **2024**, 34, 2407050.
- [11] S. B. Rajendran, K. Challen, K. L. Wright, J. G. Hardy, *J. Funct. Biomater.* **2021**, 12, 40.
- [12] M. Zhao, B. Song, J. Pu, T. Wada, B. Reid, G. Tai, F. Wang, A. Guo, P. Walczysko, Y. Gu, *Nature* **2006**, 442, 457.
- [13] E. Shirzaei Sani, C. Xu, C. Wang, Y. Song, J. Min, J. Tu, S. A. Solomon, J. Li, J. L. Banks, D. G. Armstrong, *Sci. Adv.* **2023**, 9, eadf7388.
- [14] Y. Liu, G. Dzidotor, T. T. Le, T. Vinikoor, K. Morgan, E. J. Curry, R. Das, A. McClinton, E. Eisenberg, L. N. Apuzzo, K. T. M. Tran, P. Prasad, T. J. Flanagan, S. W. Lee, H. M. Kan, M. T. Chorski, K. W. H. Lo, C. T. Laurencin, T. D. Nguyen, *Sci. Transl. Med.* **2022**, 14, eabif7282.
- [15] Y. W. Jiang, A. A. Trotsuk, S. M. Niu, D. Henn, K. Chen, C. C. Shih, M. R. Larson, A. M. M. Bunnell, S. Mittal, J. C. Lai, A. Saberi, E. Beard, S. Jing, D. L. Zhong, S. R. Steele, K. F. Sun, T. Jain, E. Zhao, C. R. Neimeth, W. G. Viana, J. Tang, D. Sivaraj, J. Padmanabhan, M. Rodrigues, D. P. Perrault, A. Chattopadhyay, Z. N. Maan, M. C. Leelouli, C. A. Bonham, S. H. Kwon, et al., *Nat. Biotechnol.* **2023**, 41, 652.
- [16] Q. Zhang, J. Zhu, H. Liu, X. Fei, M. Zhu, *Adv. Funct. Mater.* **2024**, 34, 2309968.
- [17] L. Li, D. Li, Y. Wang, T. Ye, E. He, Y. Jiao, L. Wang, F. Li, Y. Li, J. Ding, *Adv. Mater.* **2023**, 35, 2302997.
- [18] H. Wu, Y. Wang, H. Li, Y. Hu, Y. Liu, X. Jiang, H. Sun, F. Liu, A. Xiao, T. Chang, *Nat. Electron.* **2024**, 7, 299.
- [19] L. Wang, C. Lu, S. Yang, P. Sun, Y. Wang, Y. Guan, S. Liu, D. Cheng, H. Meng, Q. Wang, *Sci. Adv.* **2020**, 6, 50eabc6686.
- [20] P. Wu, P. Chen, C. Xu, Q. Wang, F. Zhang, K. Yang, W. Jiang, J. Feng, Z. Luo, *Nano Energy* **2022**, 102, 107707.
- [21] F. Jin, T. Li, T. Yuan, L. Du, C. Lai, Q. Wu, Y. Zhao, F. Sun, L. Gu, T. Wang, *Adv. Mater.* **2021**, 33, 2104175.
- [22] R. Qiu, X. Zhang, C. Song, K. Xu, H. Nong, Y. Li, X. Xing, K. Mequanint, Q. Liu, Q. Yuan, *Nat. Commun.* **2024**, 15, 4133.
- [23] D. Xu, S. Fu, H. Zhang, W. Lu, J. Xie, J. Li, H. Wang, Y. Zhao, R. Chai, *Adv. Mater.* **2024**, 2307896.
- [24] S. B. Yang, Z. D. Yuan, T. T. Wang, J. Huang, W. Wang, T. Li, Y. Wang, W. F. Dong, F. L. Yuan, *Adv. Funct. Mater.* **2024**, 2403724.
- [25] D. K. Piech, B. C. Johnson, K. Shen, M. M. Ghanbari, K. Y. Li, R. M. Neely, J. E. Kay, J. M. Carmena, M. M. Maharbiz, R. Muller, *Nat. Biomed. Eng.* **2020**, 4, 207.
- [26] C. Zhang, C. Pan, K. F. Chan, J. Gao, Z. Yang, K. K. C. Leung, D. Jin, Y. Wang, N. Xia, Z. Ning, *Sci. Adv.* **2023**, 9, eade8622.
- [27] A. Burton, Z. Wang, D. Song, S. Tran, J. Hanna, D. Ahmad, J. Bakall, D. Clausen, J. Anderson, R. Peralta, *Nat. Commun.* **2023**, 14, 7887.

- [28] X. Chen, J. Zhang, G. Chen, Y. Xue, J. Zhang, X. Liang, I. M. Lei, J. Lin, B. B. Xu, J. Liu, *Adv. Funct. Mater.* **2022**, *32*, 2202285.
- [29] Y. Xiao, Z. Yang, B. Guo, B. Wu, R. Liu, S. Zhang, P. Zhao, J. Ruan, X. Lu, K. Liu, *Adv. Funct. Mater.* **2024**, *34*, 2313131.
- [30] A. Mubarak, B. Sarsembayev, Y. Serik, A. Onabek, Z. Kappassov, Z. Bakenov, K. Tsuchiya, G. Kalimuldina, *Energy Environ. Mater.* **2025**, *8*, e12808.
- [31] W. Liu, H. Zhao, C. Zhang, S. Xu, F. Zhang, L. Wei, F. Zhu, Y. Chen, Y. Chen, Y. Huang, *Nat. Commun.* **2023**, *14*, 4091.
- [32] H. Wu, R. Luo, Z. Li, Y. Tian, J. Yuan, B. Su, K. Zhou, C. Yan, Y. Shi, *Adv. Mater.* **2024**, *36*, 2307546.
- [33] H. Wu, X. Zhang, Z. Ma, C. Zhang, J. Ai, P. Chen, C. Yan, B. Su, Y. Shi, *Adv. Sci.* **2020**, *7*, 1903208.
- [34] F. Qi, X. Gao, Y. Shuai, S. Peng, Y. Deng, S. Yang, Y. Yang, C. Shuai, *Compos. Part B Eng.* **2022**, *237*, 109864.
- [35] P. Chansoria, E. L. Etter, J. Nguyen, *Trends Biotechnol.* **2022**, *40*, 338.
- [36] K. Nuutila, E. Eriksson, *Adv. Wound Care* **2021**, *10*, 685.
- [37] M. Yan, Z. Wu, Z. Li, Z. Li, J. Wang, Z. Hu, *Biosens. Bioelectron.* **2024**, *259*, 116365.
- [38] F. Xue, S. Zhao, H. Tian, H. Qin, X. Li, Z. Jian, J. Du, Y. Li, Y. Wang, L. Lin, *Nat. Commun.* **2024**, *15*, 864.
- [39] V. I. Egorov, I. V. Schastlivtsev, E. V. Prut, A. O. Baranov, R. A. Turusov, *J. Biomech.* **2002**, *35*, 1417.
- [40] Y. Xue, X. Chen, F. Wang, J. Lin, J. Liu, *Adv. Mater.* **2023**, *35*, 2304095.
- [41] Z. Zheng, X. Chen, Y. Wang, P. Wen, Q. Duan, P. Zhang, L. Shan, Z. Ni, Y. Feng, Y. Xue, *Adv. Mater.* **2024**, 2408538.
- [42] N. Noskovicova, R. Schuster, S. van Putten, M. Ezzo, A. Koehler, S. Boo, N. M. Coelho, D. Griggs, P. Ruminski, C. A. McCulloch, *Nat. Biomed. Eng.* **2021**, *5*, 1437.
- [43] Y. Yang, R. Z. Luo, S. Y. Chao, J. T. Xue, D. J. Jiang, Y. H. Feng, X. D. Guo, D. Luo, J. P. Zhang, Z. Li, Z. L. Wang, *Nat. Commun.* **2022**, *13*, 6908.